

Beam test results of the Intermediate Silicon Tracker for sPHENIX

C. W. Shih^{a,b,c}, G. Nukazuka^{b,c,*}, Y. Sugiyama^{d,b}, Y. Akiba^{b,c}, H. En'yo^{b,c}, T. Hachiya^{d,b}, S. Hasegawa^{e,b}, M. Hata^{d,b}, H. Imai^{f,b}, C. M. Kuo^a, M. Morita^{d,b}, I. Nakagawa^{b,c}, Y. Nakamura^{f,b}, G. Nakano^{f,b}, Y. Namimoto^{d,b}, R. Nouicer^g, M. Shibata^{d,b}, M. Shimomura^{d,b}, R. Takahama^{d,b}, K. Toho^h, M. Tsuruta^h and M. Watanabe^{d,b}

^aDepartment of Physics and Center for High Energy and High Field Physics, National Central University, No.300, Zhongda Rd., Zhongli Dist., Taoyuan City, 32001, Taiwan

^bNishina Center for Accelerator-Based Science, RIKEN, 2-1 Hirosawa, Wako, 351-0198, Saitama, Japan

^cRIKEN BNL Research Center, 20 Pennsylvania Avenue, Upton, 11973, NY, U.S.A.

^dDepartment of Mathematical and Physical Sciences, Nara Women's University, Kita-uoya-Higashimachi, Nara, 630-8506, Nara, Japan

^eAdvanced Science Research Center, Japan Atomic Energy Agency, 2-4 Shirakata Shirane, Tokai-mura, Naka-gun, 319-1195, Ibaraki, Japan

^fDepartment of Physics, Rikkyo University, 3-34-1 Nishi-Ikebukuro, Toshima, Tokyo, 171-8501, Tokyo, Japan

^gBrookhaven National Laboratory, 20 Pennsylvania Avenue, Upton, 11973, NY, U.S.A.

^hResearch Center for Accelerator and Radioisotope Science, Tohoku University, 1-2-1 Mikamine, Taihaku, Sendai, 982-0826, Miyagi, Japan

ARTICLE INFO

Keywords:

RHIC
sPHENIX
Silicon detector
Beam test
Detection efficiency

ABSTRACT

The Intermediate Silicon Tracker (INTT), a two-layer barrel silicon strip tracker, is a key component of the tracking system for sPHENIX at the Relativistic Heavy Ion Collider (RHIC) at Brookhaven National Laboratory. The INTT is designed to enable the association of reconstructed tracks with individual RHIC bunch crossings. To evaluate the performance of preproduction INTT ladders and the readout chain, a beam test was conducted at the Research Center for Accelerator and Radioisotope Science, Tohoku University, Japan. This paper presents the performance of the INTT evaluated through studies of the signal-to-noise ratio, residual distribution, spatial resolution, hit-detection efficiency, and multiple track reconstruction.

1. Introduction

1.1. The sPHENIX experiment

sPHENIX [1] is a new major detector at the Relativistic Heavy Ion Collider (RHIC) [2] at Brookhaven National Laboratory (BNL). The primary goal of sPHENIX is to study the nature of the strongly interacting quark-gluon plasma (QGP) and cold quantum chromodynamics (QCD), including proton spin physics, through high-precision and high-statistics measurements of hard-probe observables [3, 4]. Designed as a state-of-the-art jet detector, sPHENIX features barrel electromagnetic and hadronic calorimeters—available for the first time at mid-pseudorapidity at RHIC—thereby enabling fully reconstructed jet measurements. In addition, the detector includes a precision tracking system comprising four subsystems, along with a refurbished 1.4 Tesla BaBar superconducting solenoid magnet [5], supporting detailed studies of jet substructure and heavy-flavor observables. Together, these components provide full azimuthal coverage and pseudorapidity acceptance of $|\eta| < 1.1$ for collision vertices located within ± 10 cm of the nominal interaction point along the beam axis.

1.2. The Intermediate Silicon Tracker (INTT)

INTT is a two-layer barrel silicon strip tracker. The schematic drawing of INTT is shown in Fig. 1. The INTT comprises 56 silicon ladders [6]—24 in the inner barrel and 32 in the outer barrel—arranged in a cylindrical configuration around the beam pipe, with radii of approximately 7.5 cm (inner barrel) and 10 cm (outer barrel). In each barrel, the ladders are staggered in the ϕ direction to ensure full azimuthal coverage. The INTT is positioned between the MAPS-based Vertex Detector (MVTX) and the Time Projection Chamber (TPC) in sPHENIX. By providing two spatial points per track, the INTT is able to bridge tracks of the MVTX and TPC to enhance pattern recognition. In addition, the INTT plays a unique and crucial role in associating reconstructed tracks with individual RHIC bunch

*Corresponding author

✉ genki.nukazuka@riken.jp (G. Nukazuka)

ORCID(s):

crossings, thereby enabling effective out-of-time pileup discrimination and suppression, thanks to the superior timing resolution of INTT among the sPHENIX tracking detectors.

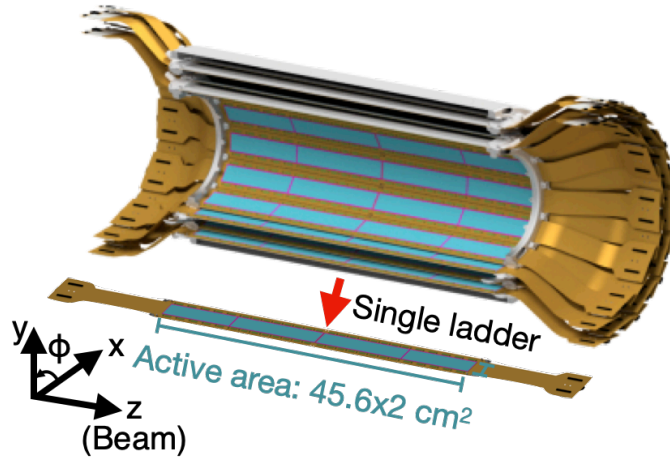


Figure 1: The schematic drawing of the INTT barrel and a ladder. The active areas of the ladders are shown as cyan boxes. The coordinate system used for the sPHENIX experiment is also shown.

Figure 2 presents a schematic drawing of an INTT ladder. An INTT ladder comprises Type-A and Type-B silicon sensors, 52 FPHX readout chips [7], two high-density interconnect (HDI) cables, and a carbon fiber composite (CFC) stave underneath the HDIs as a support structure and heat transmitter. The silicon sensor is divided into sixteen (Type-A) or ten (Type-B) blocks, read out by individual FPHX chips. Each block contains 128 silicon strips with a pitch of $78\text{ }\mu\text{m}$ and a length of 16 mm (Type-A) or 20 mm (Type-B). Details of the INTT ladder are discussed in Ref. [6]. Ladders are assembled at BNL and the Taiwan Instrumentation and Detector Consortium. Table 1 summarizes key specifications of the INTT ladder.

When a charged particle traverses a silicon sensor of INTT, electron-hole pairs are created. The corresponding FPHX chip reads the analog signal and converts it to digital information. The signal amplitude is digitized using a 3-bit analog-to-digital converter (ADC), which comprises eight programmable comparators. The threshold of each comparator, hereinafter referred to as the digital-to-analog converter (DAC) value, can be set within a range of 0 to 255. The amplitude of the analog signal is compared against all comparators, and the digitized value is determined by the index of the comparator with the highest threshold exceeded. Signals with amplitudes below the lowest comparator threshold are discarded. The digitized signal is sent to the readout card (ROC) through the HDI cable and an extension cable. The left and right halves of the INTT ladder, as illustrated in Fig. 2, have the same structure but are operated independently.

1.3. The beam test

A silicon tracking detector is expected to have a good signal-to-noise ratio (>10) and a high hit-detection efficiency ($>99\%$). A beam test was conducted to evaluate the performance of the INTT ladder and its readout chain towards the last phase of R&D. The schematic diagram of the beam test setup is shown in Fig. 3. A dedicated telescope—comprising four preproduction INTT ladders evenly spaced in a dark box—was built for the beam test at the Research Center for Accelerator and Radioisotope Science¹ (RARiS) [8], Tohoku University, Japan. Trigger scintillators, matching the dimensions of the silicon sensors on half of a ladder, were installed at the upstream and downstream ends of the INTT telescope. The coincidence signal of the two trigger scintillators was used as the trigger signal. A fingertip-sized scintillator was placed in front of the upstream trigger scintillator, but its data was not included in the analysis. The INTT telescope was installed on the -23° beamline in the gamma-ray irradiation hall of RARiS. The positron beam with a momentum of $1\text{ GeV}/c$ was produced by the interaction of the primary gamma-ray beam with a $200\text{ }\mu\text{m}$ -thick tungsten production target.

During the beam test, the right halves of the INTT ladders were operated for data collection, except for the most upstream ladder, due to a bias voltage issue. The remaining three ladders showed good performance and are denoted

¹Formerly known as the research center for ELection PHoton science, ELPH.

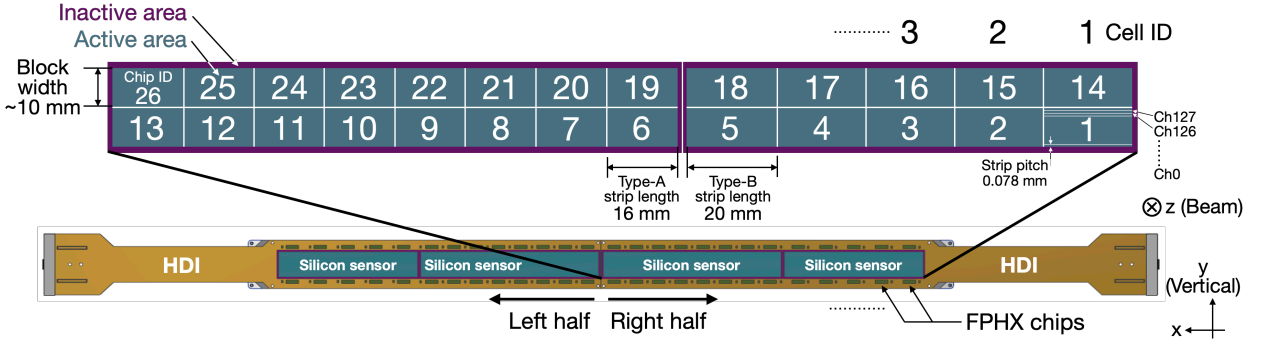


Figure 2: The schematic drawing of an INTT ladder with sensors facing up. An INTT ladder consists of two types of silicon sensors, FPHX chips, HDI cables, and a CFC stave. The sensors are divided into 16 (Type-A) and 10 (Type-B) blocks read out by individual FPHX chips. A silicon block has 128 strips oriented horizontally with a pitch of $78\mu\text{m}$ and a length of 16 mm (Type-A) or 20 mm (Type-B). The coordinate system used in the beam test is also shown.

as L_0 , L_1 , and L_2 hereafter. In each FPHX chip, the lowest comparator threshold was set to a DAC value of 15, unless otherwise specified. The trigger signals (processed by NIM logic modules) and the INTT hit data were sent to a PHENIX FVTX front-end module (FEM) [9]. The FEM stores the INTT data only when an active trigger signal is present. The data were collected using a data acquisition system developed with the PCIe-6536B (National Instruments Co.) running on a Windows 10 operating system.

We note that the INTT operational configuration used in the beam test was a prototype setup and differed slightly from the final configuration for the sPHENIX detector. In the beam test, a 40-centimeter flexible printed circuit (FPC)-based cable was used to transmit signals between the HDI and ROC during the measurements, except for one run used for the hit-detection efficiency study (as discussed in Section 2.4). In this run, a 1.3-meter prototype bus-extender (BEX) cable [10] was additionally connected to L_1 following the FPC-based cable. This measurement was intended to assess the reliability of data transmission through the BEX. Data readout was performed using an FEM. In the final INTT setup, a μ -coaxial cable [6] and a shorter 1.11-meter bus-extender cable are employed for each HDI-to-ROC connection, with data read out by the FELIX board [11]. We also note that the bias voltage applied to the sensors during the beam test was 50 V, slightly below the full depletion voltage of approximately 62 V. For INTT during the sPHENIX data taking, a nominal operating bias voltage of 100 V is applied.

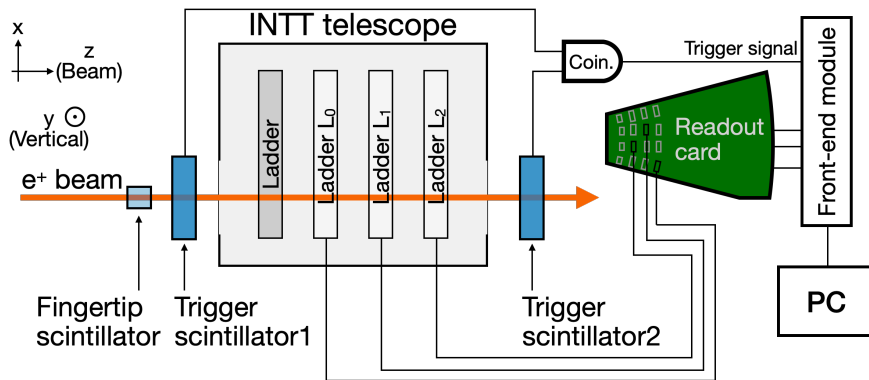


Figure 3: The schematic diagram of the setup for the INTT beam test at RARiS. The INTT telescope, containing four evenly spaced INTT preproduction ladders, was located on the positron beamline. Two trigger scintillators were installed upstream and downstream of the INTT telescope, respectively. A fingertip-sized scintillator was placed in front of the upstream trigger scintillator, but its data was not included in the analysis. The x-, y-, and z-axes used in the beam test are also shown.

Table 1
Specification of the INTT ladder.

Element	Value
Radiation length	1.14% [X/X_0]
Active area	$45.6 \times 2 \text{ cm}^2$
Number of channels	6,656
Channel strip pitch	78 μm
Channel strip length	16 mm (Type-A sensor) 20 mm (Type-B sensor)

2. Analysis and results

The section is organized into four topics: the signal-to-noise ratio (Section 2.2), the residual distribution and the INTT spatial resolution (Section 2.3), the hit-detection efficiency (Section 2.4), and the multiple track reconstruction (Section 2.5). Aspects of the analysis common to the topics are introduced jointly (Section 2.1), while topic-specific methods and results are discussed in the respective subsections.

2.1. Common analysis components

Three noisy channels found in L_2 are excluded from the analysis². Vertically adjacent blocks in each ladder, for example, chips 1 and 14 in Fig. 2, are treated as one cell. Amplitudes of the recorded INTT hits are converted to the predefined threshold setting of the corresponding comparator, after which clustering is performed. In a given cell of a ladder, groups of vertically adjacent hits are treated as clusters. The cluster's x-position is assigned as the same cell index, while its y-position, Y , is determined using the weighted average method:

$$Y = \sum_{i=1}^n (e_i \cdot y_i) / \sum_{i=1}^n e_i,$$

where n is the number of hits in the cluster, and e_i and y_i denote the converted amplitude and y-position of the i -th hit. The cluster amplitude is defined as the sum of the e_i values of the hits in the cluster. These clusters represent the total energy deposited by a charged particle traversing an INTT ladder and carry information about its location. The resulting clusters serve as input to subsequent analyses.

To compare the INTT ladder performance with simulation, a GEANT4 [12] model is developed based on the INTT beam test setup, including the INTT telescope and the scintillator configuration. In addition, the particle-gun generator is configured according to the beam characteristics of the -23° beamline in the gamma-ray irradiation hall of RARiS.

The tracking analysis begins in Section 2.3. It includes correlating clusters across multiple ladders in the selected cell and correcting the ladder misalignment along the vertical axis. Given the setup of the INTT telescope, a residual can be defined as $r = (Y_{L_1} + C_{L_1}) - Y_{\text{pred}}$, where Y_{L_1} is the position of the L_1 cluster in the y-axis, C_{L_1} is the misalignment correction for L_1 relative to L_0 and L_2 , and Y_{pred} is the expected y-position for the L_1 cluster, obtained by a linear interpolation of L_0 and L_2 clusters.

The C_{L_1} is determined using events with exactly one cluster in the selected cell of each ladder. In addition, the absence of clusters in cells adjacent to the selected one is required to account for potential misalignment along the horizontal axis. The r is then calculated with C_{L_1} set to zero. The resulting distribution of a representative cell is shown in Fig. 4. The mean of a Gaussian function fitted to the distribution is offset from zero by 0.298 mm, indicating that L_1 is positioned slightly lower relative to L_0 and L_2 in the vertical axis. Accordingly, C_{L_1} is assigned to be -0.298 mm, the negative Gaussian mean, to correct for the misalignment of L_1 .

2.2. Signal-to-noise ratio

The signal-to-noise ratio is one of the key parameters for evaluating the performance of a tracking detector and ensuring the reliability of the recorded data. The signal-to-noise ratio is $R \equiv S/N$, where S is the most probable energy deposition of minimum ionizing particles, and N is the root mean square of the noise distribution of the system. The R can be extracted from an energy-deposit distribution. As a trade-off for the low power consumption, the energy

²The noisy channels are far away from the beam-spot.

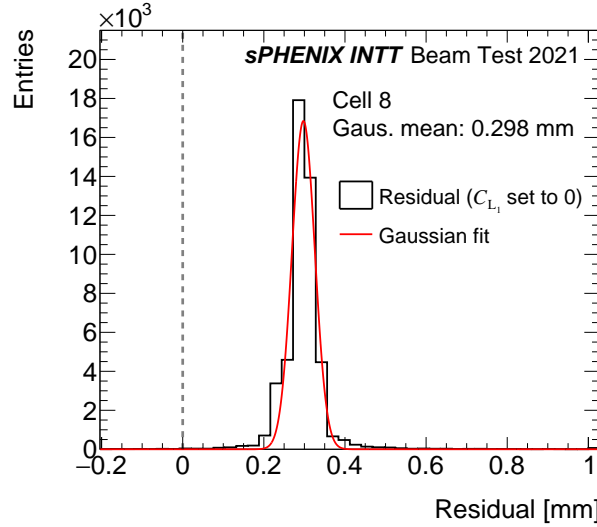


Figure 4: The distribution filled by r with C_{L_1} set to zero for a representative cell. The mean of the Gaussian function fitted to the distribution indicates the amount of misalignment of L_1 relative to L_0 and L_2 .

resolution of the FPHX chip is limited by its 3-bit ADC, which is insufficient to study the energy-deposit distribution with high precision. To address this, a series of eight narrow-range measurements, with threshold increments as small as 4 DAC, referred to as a DAC scan, was conducted. The measurement ranges of the DAC scan runs are summarized in Table 2. This approach allows each measurement to cover a slightly different region of the energy-deposit distribution, with some overlap between adjacent ones, enabling the full energy-deposit spectrum to be mapped with high precision.

Ladders L_0 and L_2 are included in this study. Events with at most one cluster per ladder are selected. The analysis focuses on clusters in the beam-spot region of the selected events. Amplitudes of single-hit clusters (clusters consisting of a single activated channel, with no adjacent channels registering a hit) are binned into separate histograms for each measurement. Scaling factors derived from overlapping bins are applied to the histograms to normalize the eight measurements and construct the full energy-deposit distribution, as illustrated in Fig. 5.

For each of L_0 and L_2 , the eight corresponding distributions are merged to produce an integrated distribution, referred to hereafter as E_0 and E_2 . They are then statistically combined to obtain the average distribution, representing the average energy-deposit distribution of the INTT ladders, as shown in Fig. 6. Deviations of E_0 and E_2 from the average are assigned as systematic uncertainties (yellow boxes). A clear signal component followed by a steeply falling noise component is observed. The average distribution, as well as E_0 and E_2 , is fitted with a Landau-Gaussian convolution function (Landau \otimes Gaussian) [13] for the signal component, plus two Gaussian functions with peaks fixed at the origin for the noise component. Taking the variation of the Landau most probable values (MPV) of E_0 and E_2 as a source of systematic uncertainty, the most probable energy deposition of minimum ionizing particles for the INTT ladders is measured to be a DAC value of 73.23 ± 0.20 (stat.) ± 1.71 (syst.). The noise width is determined as the average of the widths of the two Gaussian functions fitted to the average distribution, weighted by their respective areas. The resulting noise width corresponds to a DAC value of 4.56 ± 0.16 . The signal-to-noise ratio of the INTT ladders is measured to be greater than 15.1, exceeding the conventional requirement.

2.3. Residual distribution

To obtain the residual distribution, a set of event selection criteria is applied. Events with one cluster per ladder, located in the selected cell, are retained. Additionally, to ensure the clusters originate from beam particles, the L_0 and L_1 clusters must lie within the beam-spot, and the vertical slope of the line connecting them is required to be close to zero, matching that of the beam direction. Residuals are calculated as the outcome of tracking, in which clusters in three ladders are correlated. The results are shown in Fig. 7. The data exhibit a symmetric distribution with steeply falling tails, owing to the low material budget of the INTT ladders. The L_1 misalignment measured from the data was incorporated into the GEANT4 model. A distribution obtained from the simulation through the same analysis procedure

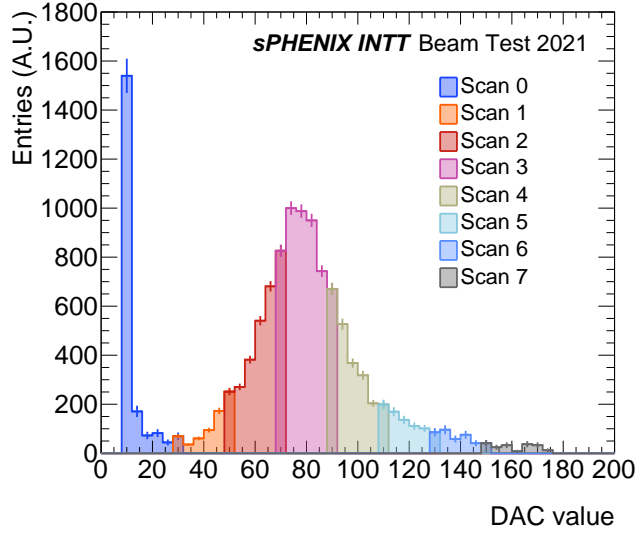


Figure 5: The energy-deposit distribution, constructed by the eight sequential measurements (histograms with different colors) after applying scaling factors, for a representative ladder (L_0).

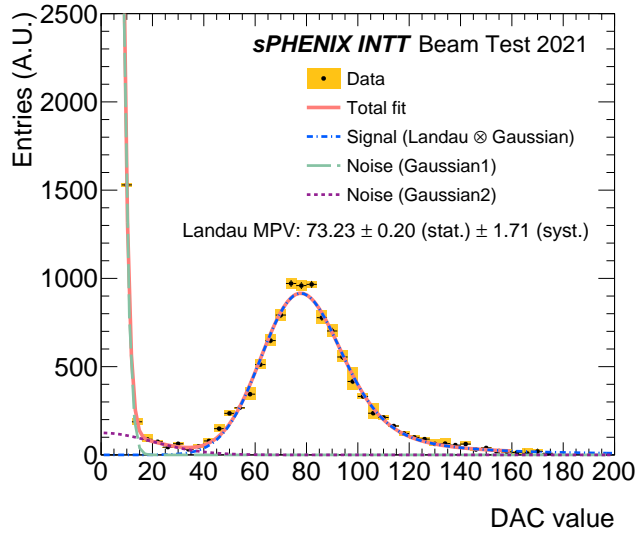


Figure 6: The energy-deposit distribution of the INTT ladders fitted by a Landau-Gaussian convolution function for the signal component, plus two Gaussian functions for the noise component. The vertical extent of each yellow box represents the systematic uncertainty of the ladder variation, while the vertical bar shows the statistical uncertainty.

was prepared for comparison. The residual distributions in data and simulation are in agreement, which indicates good control of the implemented geometry and material configuration.

2.3.1. Spatial resolution

We note that it is not straightforward to extract the spatial resolution of the INTT ladder along the y-axis directly from the residual distribution of a full GEANT4 simulation, because the residual distribution includes contributions from the intrinsic resolution of the INTT ladder (σ_{lad}) and the effect of multiple Coulomb scattering. Therefore, an analytical approach is employed, as described below.

Table 2

The measurement ranges of DAC scan runs used for constructing the INTT energy-deposit distribution.

Scan	Minimum	Maximum
0	8	36
1	28	56
2	48	76
3	68	96
4	88	116
5	108	136
6	128	156
7	148	176

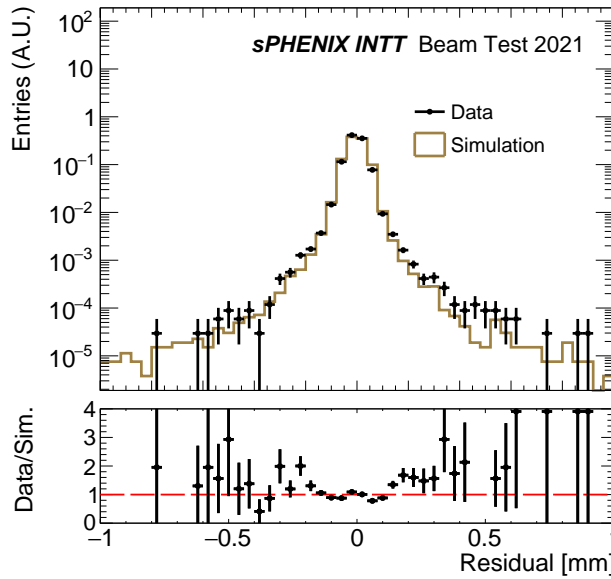


Figure 7: Residual distributions obtained from data (solid black circles) and simulation (brown line). The bottom panel presents the ratio of the data to the simulation.

The resolution of Y_{pred} ($\sigma_{Y_{\text{pred}}}$) is defined as:

$$\sigma_{Y_{\text{pred}}}^2 = \frac{1}{2} \cdot \sigma_{\text{lad}}^2,$$

following the formula outlined in Ref. [14]. The measured residual distribution effectively corresponds to the residual distribution of the multiple Coulomb scattering (MS) convolved with a Gaussian distribution of width $\sqrt{3/2} \cdot \sigma_{\text{lad}}$. This Gaussian distribution reflects the finite spatial resolution of the three INTT ladders in the INTT telescope.

A scan is performed by convolving the simulated residual distribution of the multiple Coulomb scattering with a series of Gaussian functions of increasing width ($\text{MS} \otimes \text{Gaus}$), and the resulting distributions are compared with the data. A representative example is given in Fig. 8. The chi-square test is employed to quantify the agreement, using the central six bins that contain over 98% of the entries. The reduced χ^2 as a function of the Gaussian width is shown in Fig. 9. A second-order polynomial function (red line) is fitted to the curve. A local minimum at $22.07 \mu\text{m}$ is observed, corresponding to an INTT spatial resolution, σ_{lad} , of $18 \mu\text{m}$.

2.4. Hit-detection efficiency

The hit-detection efficiency of silicon tracking detectors, denoted as ϵ , is generally expected to be high ($>99\%$) due to their favorable signal-to-noise ratio. Typically, ϵ of a device under test (DUT) is evaluated using a tracking

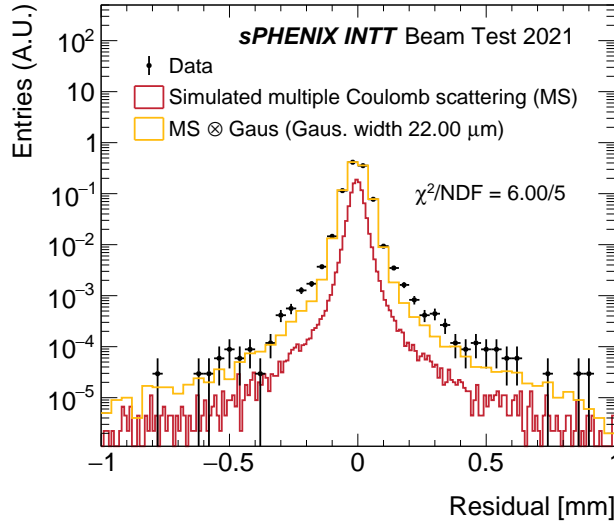


Figure 8: A representative example of a residual distribution (yellow line), obtained by convolving a simulated residual distribution of multiple Coulomb scattering (red line) with a Gaussian distribution of width $22\mu\text{m}$, compared with the data distribution (solid black circles). The agreement is quantified by a chi-square test, using the central six bins that contain over 98% of the entries.

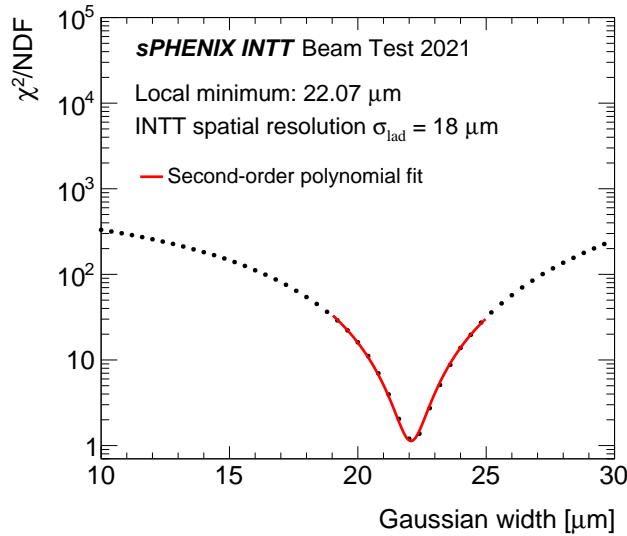


Figure 9: The reduced χ^2 as a function of the Gaussian width. A second-order polynomial function (red line) is fitted to the curve to obtain the local minimum at $22.07\mu\text{m}$, corresponding to an INTT spatial resolution of $18\mu\text{m}$.

system. The DUT is positioned between the upstream and downstream sectors of the tracking system. When a good track is reconstructed, the presence or absence of a corresponding hit in the DUT allows for an assessment of its detection efficiency, as the track is known to have traversed the DUT. In this beam test, L_0 and L_2 are used for track reconstruction, while L_1 is designated as the DUT, and its hit-detection efficiency is measured.

Since tracks are reconstructed using only two ladders (L_0 and L_2), stringent event selection criteria are applied to ensure the purity of reconstructed tracks. The cell on the beam-spot is chosen as the baseline. To minimize track ambiguity and account for potential ladder misalignment along the horizontal axis, events are required to have exactly one cluster in the selected cell of L_0 and L_2 , and no clusters in the adjacent cells of any of the three ladders. In

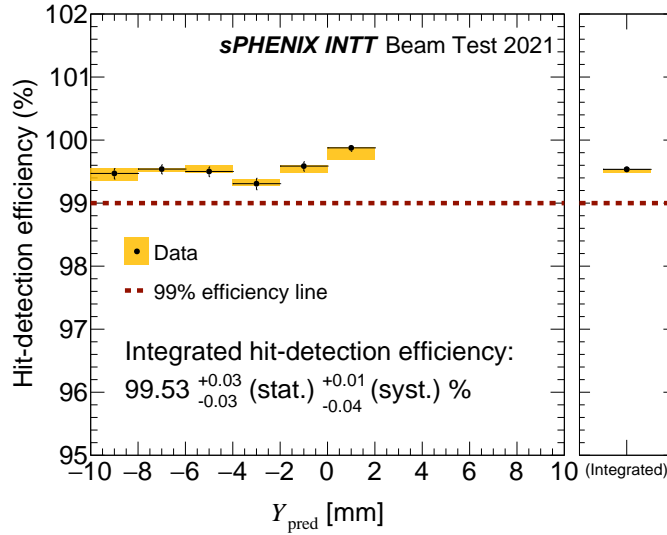


Figure 10: The hit-detection efficiency of L_1 as a function of Y_{pred} (left panel), as well as the integrated result (right panel). The vertical extent of each yellow box represents the total systematic uncertainty, while the vertical bar shows the statistical uncertainty. The red dashed line represents an efficiency of 99%.

addition, events in which the smallest-amplitude cluster occurs in L_0 or L_2 are discarded to suppress noise contribution. Furthermore, the vertical slope of the line connecting the clusters of L_0 and L_2 is required to be close to zero to align with the beam direction, and the y-positions of these clusters must be within the beam-spot region to ensure the reconstructed tracks originate from the beam.

Events that pass these criteria are considered to contain a good track. Y_{pred} is then obtained from the track, and clusters in the selected cell of L_1 are examined. If a cluster is found in L_1 and its absolute residual is within 0.7 mm, the event is classified as a successful detection of a particle hit in L_1 . The residual criterion is determined from a simulation study, in which the detection efficiency exceeds 99.995% for $|r| > 0.7$ mm. The hit-detection efficiency is defined as:

$$\epsilon = \frac{\text{Events with } L_1 \text{ cluster matching to track}}{\text{Events with good track}}.$$

Systematic uncertainties affecting the efficiency measurement are evaluated. The stability of detector components is assessed by performing the analysis with the cell having the second-highest cluster count. The sensitivity of the selection for the track's vertical slope is examined by varying the criterion in the selection. For each source, the resulting deviation in hit-detection efficiency is quoted as a systematic uncertainty.

Figure 10 presents the hit-detection efficiency of L_1 as a function of Y_{pred} (left panel), as well as the integrated result (right panel). The total systematic uncertainty (yellow boxes) is obtained by summing all sources in quadrature under the assumption that they are independent and uncorrelated. The data cover the y-axis range from -10 mm to $+2$ mm, partially spanning the sensor's full extent (-10 mm to $+10$ mm). While the entire sensor is not covered, the data reach the edge on one side. Within the reported range, ϵ stays above 99%. The integrated hit-detection efficiency of L_1 is measured to be $99.53^{+0.03}_{-0.03}$ (stat.) $^{+0.01}_{-0.04}$ (syst.)%.

The analysis is also performed using another run with the nominal cabling configuration as a reference. The hit-detection efficiencies obtained from the two runs differ by less than 0.1%, indicating excellent reliability of the data transmission through the BEX.

2.5. Multiple track reconstruction

The performance of multiple track reconstruction is demonstrated using a special run with an additional 1 cm-thick lead plate ($1.78 X/X_0$) placed 40 cm upstream of the INTT telescope. The positron beam is delivered and directed onto the lead plate, inducing a particle shower. Secondary particles from this interaction are expected to traverse the INTT telescope. All 13 cells are included in this analysis to maximize the detector acceptance. The track-finding procedure

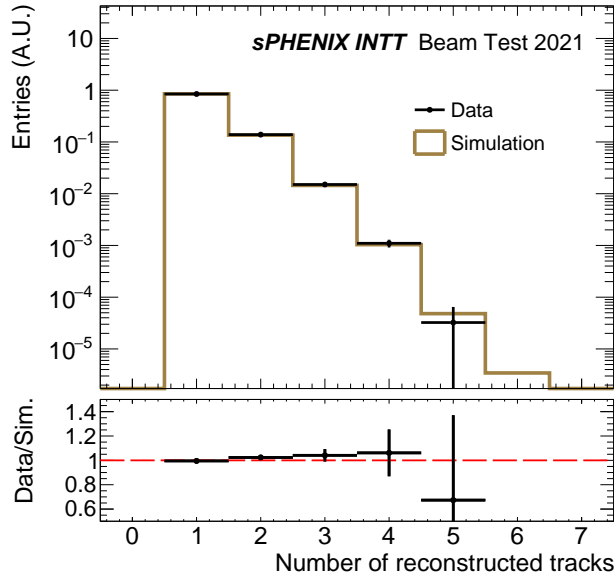


Figure 11: Distributions of the number of reconstructed tracks using the full acceptance available for the beam test in data (solid black circles) and simulation (brown line). The bottom panel presents the ratio of the data to the simulation.

starts by looping over all clusters in a given cell across the three INTT ladders. The most linear combination, quantified by a straight-line fit, is selected. If the residual r of the chosen combination is within ± 0.7 mm, it is classified as a good track. The associated clusters are removed from the rest of the track-finding for a given event, and the procedure is repeated iteratively until no further combination satisfies the residual criterion.

Figure 11 shows the distribution of the number of reconstructed tracks per event. Given the full acceptance available for the beam test, up to five tracks can be reconstructed from a single event. The same distribution from a dedicated simulation sample using the same analysis procedure is presented for comparison. The data are in good agreement with the simulation, serving as a benchmark measurement that validates the tracking performance of the INTT under high-multiplicity conditions.

3. Conclusion

The performance of the Intermediate Silicon Tracker (INTT) was evaluated using a positron beam with a momentum of 1 GeV/c at RARiS. The INTT ladders demonstrated a signal-to-noise ratio exceeding 15.1, and a hit-detection efficiency above 99% in the reported range along the vertical axis. The measured residual distribution showed strong agreement with the simulation, indicating good control of the ladder geometry and material configuration, as well as high data quality. The spatial resolution of the INTT, evaluated from the residual distribution, was measured to be 18 μm . Multiple track reconstruction performance was further benchmarked using a positron-induced particle shower, with data and simulation in good agreement. These results confirm that the INTT meets the performance requirements for precision tracking. The INTT was installed and commissioned in the sPHENIX detector in 2023 and has since been collecting data stably with p+p and Au+Au collisions [15], leading to the first physics results from sPHENIX [16].

Acknowledgments

We express our gratitude to RARiS and the staff for the stable operation of the accelerators during the beam test. We are grateful to the sPHENIX collaboration for their support and assistance during various phases of the INTT ladder and readout cable developments. We thank the PHENIX FVTX experts for providing essential documentation and devices. We thank Prof. Takatsugu Ishikawa for serving as the liaison between RARiS and our group during the

beam test and for providing the simulation setup used to model the beam characteristics of the -23° beamline of the gamma-ray irradiation hall of RARiS.

We acknowledge support from the Ministry of Education, Culture, Sports, Science, and Technology and the Japan Society for the Promotion of Science (Japan); Office of Nuclear Physics in the Office of Science of the Department of Energy (U.S.A.); National Science and Technology Council and the Ministry of Education (Taiwan).

References

- [1] A. Adare et al. (PHENIX Collaboration). An Upgrade Proposal from the PHENIX Collaboration, 2015. URL: <https://arxiv.org/abs/1501.06197>, arXiv:1501.06197.
- [2] M. Harrison, T. Ludlam, and S. Ozaki. RHIC project overview. *Nucl. Instrum. Meth. A*, 499(2):235–244, 2003. doi:10.1016/S0168-9002(02)01937-X.
- [3] USDOE Office of Science (SC) (United States). Reaching for the Horizon: The 2015 Long Range Plan for Nuclear Science, 09 2015. URL: <https://www.osti.gov/biblio/1296778>.
- [4] R. Belmont et al. Predictions for the sPHENIX physics program. *Nucl. Phys. A*, 1043:122821, 2024. doi:10.1016/j.nuclphysa.2024.122821.
- [5] B. Aubert et al. (BABAR Collaboration). The BABAR detector. *Nucl. Instrum. Meth. A*, 479(1):1–116, 2002. URL: <https://www.sciencedirect.com/science/article/pii/S0168900201020125>, doi:10.1016/S0168-9002(01)02012-5.
- [6] Y. Akiba et al. The Ladder and Readout Cables of Intermediate Silicon Strip Detector for sPHENIX, 2025. URL: <https://arxiv.org/abs/2503.09105>, arXiv:2503.09105.
- [7] J. R. Hoff, T. N. Zimmerman, R. J. Yarema, J. S. Kapustinsky, and M. L. Brookes. FPHX: A new silicon strip readout chip for the PHENIX experiment at RHIC. In *2009 IEEE Nuclear Science Symposium Conference Record (NSS/MIC)*, pages 75–79, 2009. doi:10.1109/NSSMIC.2009.5401873.
- [8] H. Hama. ELPH, Towards Scientific Research Core Based on Electron Accelerators. In *AAPPS Bull.*, volume 30 (2), pages 41–45, 2020. URL: <https://aappsbulletin.org/cop/bbs/000000000000/selectArticleDetail.do?nttId=4348>.
- [9] C. Aidala et al. The PHENIX Forward Silicon Vertex Detector. *Nucl. Instrum. Meth. A*, 755:44–61, 2014. URL: <https://www.sciencedirect.com/science/article/pii/S0168900214004124>, doi:10.1016/j.nima.2014.04.017.
- [10] T. Kondo et al. Development of Long and High-Density Flexible Printed Circuits. *Transactions of The Japan Institute of Electronics Packaging*, 15:E21-007-1–E21-007-10, 2022. doi:10.5104/jiepeng.15.E21-007-1.
- [11] J. Anderson et al. FELIX: a PCIe based high-throughput approach for interfacing front-end and trigger electronics in the ATLAS Upgrade framework. *Journal of Instrumentation*, 11(12):C12023, dec 2016. URL: <https://dx.doi.org/10.1088/1748-0221/11/12/C12023>, doi:10.1088/1748-0221/11/12/C12023.
- [12] S. Agostinelli et al. (GEANT4 Collaboration). GEANT4 - A Simulation Toolkit. *Nucl. Instrum. Meth. A*, 506:250–303, 2003. doi:10.1016/S0168-9002(03)01368-8.
- [13] S. Hancock, F. James, J. Movchet, P. G. Rancoita, and L. VanRossum. Energy loss and energy straggling of protons and pions in the momentum range 0.7 to 115 GeV/c. *Phys. Rev. A*, 28:615–620, Aug 1983. URL: <https://link.aps.org/doi/10.1103/PhysRevA.28.615>, doi:10.1103/PhysRevA.28.615.
- [14] L. Li, M. Dong, Z. Gao et al. Effect of multiple coulomb scattering on the beam tests of silicon pixel detectors. *NUCL SCI TECH*, 35:83, 2024. doi:10.1007/s41365-024-01447-9.
- [15] C. W. Shih. Intermediate Silicon Tracker in sPHENIX at RHIC, 2025. URL: <https://arxiv.org/abs/2508.06536>, arXiv:2508.06536.
- [16] M. I. Abdulhamid et al. (sPHENIX Collaboration). Measurement of charged hadron multiplicity in Au+Au collisions at $\sqrt{s_{NN}} = 200$ GeV with the sPHENIX detector. *Journal of High Energy Physics*, 2025:75, 2025. doi:10.1007/JHEP08(2025)075.